Bubble Coalescence Dynamics

Richard L. Stover, Charles W. Tobias, and Morton M. Denn
Energy and Environment and Materials Sciences Divs., E. O. Lawrence Berkeley National Laboratory and Dept. of Chemical Engineering, University of California, Berkeley, Berkeley, CA 94720

Coalescence of electrolytically-generated, 50- to 600- μm-diameter gas bubbles was observed using an optical technique that employs a linear photodiode array to detect interface movement with a resolution of 10^{-6}s. When two bubbles coalesce, the surface energy that is released causes interface velocities of 2 to 4 m/s; these are followed by large-amplitude damped oblate–prolate oscillations. Within the viscosity range studied, the oscillation period is insensitive to the viscosity and damping is insensitive to surface tension, in agreement with a scaling analysis based on a damped harmonic oscillator. Surface waves are superimposed on the motion. Finite-element solutions of the free-surface, nonlinear Navier-Stokes equations are consistent with the experiments.

Introduction

Bubble coalescence causes vigorous motion in the surrounding liquid and has a major effect on mass transfer. In electrochemical systems, coalescence further affects overpotential behavior and ohmic resistance. The dynamics of thinning of the liquid film between two approaching bubbles just prior to coalescence has been addressed by DeVries (1958), Marrucci (1969), Oolman and Blanch (1986), and Chi and Leal (1989), while Charles and Mason (1960), Frankel and Mysels (1969), Patzek and coworkers (1991), Basaran (1992), and Egan and Tobias (1994) have analyzed interfacial motion after film rupture. The qualitative impact of bubble coalescence on macroscopic fluid motion and mass transfer has been studied by Janssen and Hoogland (1973), Putt (1975), Sides and Tobias (1985), and Dees and Tobias (1987).

Little is known quantitatively about coalescence of gas bubbles in the 20- to 1,000-μm-diameter range characteristic of electrolytic systems, where the events typically occur on a millisecond time scale. Egan and Tobias (1994) observed interfacial motion in one dimension during coalescence of bubbles with diameters greater than 500 μm using a linear photodiode array with a digital output and self-triggering capability at sampling rate of up to 10^6 samples/s, but they were unable to study smaller diameters because of optical resolution and detector sensitivity. We have refined their method to quantify the interfacial velocities and shape changes associated with the coalescence of electrolytic gas bubbles with diameters as small as 50 μm, and we have investigated the effects of bubble size, electrolyte viscosity, and surface tension. The effects of the system parameters are captured by a simple scaling analysis, while the detailed surface mechanics are in general agreement with a finite-element simulation of the interface shape and local fluid motion immediately following film rupture.

Experimental Apparatus

A laser projection apparatus was constructed to project an image of the shadow of two coalescing bubbles onto a photodiode array detector designed to sense the rapid transition from light to dark produced by the passage of a bubble interface. The optical system is shown in Figure 1. The Lexel model 75 argon ion laser emits up to 80 mW of 488-nm laser light as measured with a Coherent 2000 power/energy meter. The beam expander, which consists of 12.5- and 50-mm-focal-length spherical lenses, collimates the beam and expands it by a factor of 3.8. The diameter of the expanded beam is 3.2 mm. The beam expander is followed by the beam sheet lens, a 25.4-mm-focal-length vertically-oriented cylindrical lens; this lens is focused on the axis of the centers of the two coalescing bubbles, narrowing the beam to less than 10 μm at the focal point. A horizontally oriented, 12.7-mm-focal-length cylindrical lens magnifies the image of the coalescing bubbles in the vertical direction. The final lens in the sequence, the 50-mm-focal-length compensating lens, collects the light diverging from the beam sheet lens and projects it onto the detector. All lenses used are achromatic and were supplied by Melles Griot.

Correspondence concerning this article should be addressed to M. M. Denn at denn@socrates.berkeley.edu.
Present address of R. L. Stover: IBM Storage Systems Division, 5600 Cottle Road, San Jose, CA 95193.
C. W. Tobias is deceased.

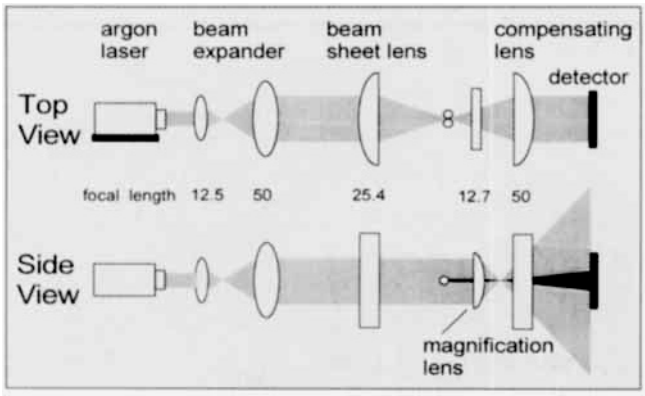

Figure 1. Optical system.

Focal lengths shown (in mm) are those of lenses used for the 150- and 375-μm bubble.

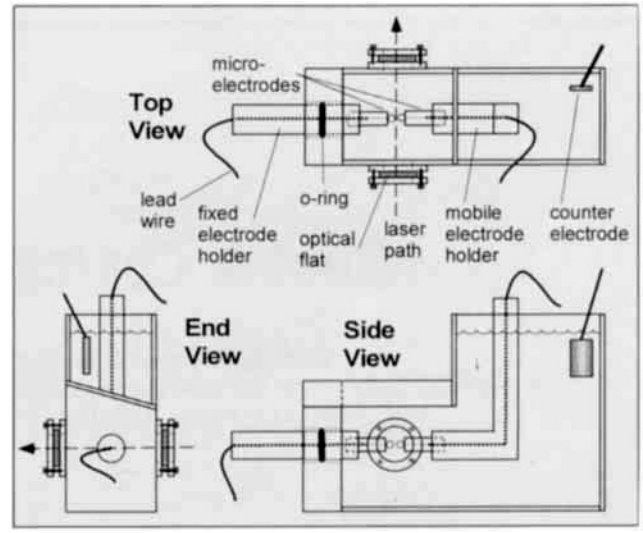

Figure 2. Electrolytic cell (not to scale).

A prototype of the detector was described by Egan and Tobias (1994). The system utilizes a Hamamatsu S4114 series high-speed linear photodiode array, which consists of sixteen 0.09 cm elements on 0.1 cm centers capable of responding to a light-to-dark transition in less than 50 ns. The 16 elements are connected in parallel through 16 high-speed video amplifiers to boost the weak diode output by 50 times to over 4.0 V. Each detector element output is adjusted by a resistor to eliminate any offset bias. The amplified analog signals then go through four Maxxim four-channel high-speed comparators that convert them to digital signals by referring to adjustable reference voltages. The binary signals are stored in the 4 kB on-board memory (256 time steps over 16 channels). The data from each new time step overwrite the oldest record. The data-acquisition logic is equipped with a self-triggering capability, and the storage sequence is initiated by the coalescence event. When the shadow passes one of the two center elements, the logic signals a computer (IBM-PC) to download the data to disk storage and to reset the trigger. With this triggering protocol, the detector system is able to record the location of the interface as a function of time both before and during a coalescence event. The detector circuitry includes a 1-MHZ crystal oscillator and a 100-increment dwell setting, which permits sampling rates from 10^3 to 10^6 16-element samples per second. A rotating beam chopper was used to generate a constant velocity of 2 m/s, which is approximately the velocity of a coalescence transient; each element responded equally, and the slope of the position-time data equaled the known velocity of the chopper blade.

The electrolytic cell used to generate bubbles is shown in Figure 2. The 20-mL electrolytic cell was constructed with 3.2-mm-thick acrylic resin walls joined together using methylene chloride. To minimize optical distortion along the laser path, 3.2-mm-thick, 1-cm-dia. glass optical flats were pressed against open ports drilled in the cell walls. To permit the magnification lens to approach the microelectrodes closely, the distance from the microelectrodes to the second optic flat along the laser path was 1.0 cm. The microelectrodes consisted of 127-μm-dia. platinum wires thermally sealed inside 3-mm-dia. soft glass tubes. Insulated copper wires contacted the platinum wires by conducting epoxy and connected the microelectrodes to the current source. The microelectrode faces were polished to a mirror finish using 0.25-μm Metadi diamond polishing compounds and a Beuhler metallurgical polishing wheel. The acrylic resin electrode holders, one fixed and one movable relative to the cell, fit tightly around the microelectrodes. A 100-mm^2 platinum sheet welded to a 1-mm-diameter platinum wire was used as a counterelectrode.

Current was supplied to the electrodes with a Princeton Applied Research 173 potentiostat operated in galvanostatic mode. Gas bubbles were generated by electrolysis of the water. For the generation of hydrogen bubbles, the cathodic current was divided between the microelectrodes with an adjustable potentiometer while the sheet electrode served as the anode. For the generation of oxygen bubbles, the anodic current was divided between the microelectrodes. To generate one oxygen and one hydrogen bubble, one microelectrode was used as the positive electrode and the other as the negative electrode; the platinum sheet was not required. By adjusting the total current to the cell using the potentiostat, and the relative current to each electrode using the potentiometer, two equal-sized bubbles were grown at approximately the same slow rate, with the time from nucleation to coalescence typically about 5 to 10 min. The bubbles remained attached to the electrodes until they were detached by the violent motion of the interface during the coalescence event. Bubble evolution was observed through the top of the cell with the microscope at magnifications of 100 to 750.

The electrolyte used in most experiments was aqueous 1-M H_2SO_4, but some experiments were conducted in aqueous 2-M KOH to test the effect of pH. The electrolyte was prepared by combining volumetrically measured amounts of deionized water and weighed amounts of reagent grade chemicals. The water was purified with a Barnstead NANO Pure system to a resistivity of at least 15 megaohm-cm. The kinematic viscosity was increased by the use of dextran T40 polysaccharide; the kinematic viscosity was measured with a capillary viscometer to the nearest 0.05×10^{-2} cm^2/s, and a variable shear rate viscometer was used to confirm that the dextran-acid solutions were Newtonian up to shear rates of 100 s^{-1}. The surface tension was lowered by adding 2-hexanol; surface tensions were measured with a Wilhelmy plate apparatus to the nearest 3 mN/m. Used electrolyte was

tested to determine if the viscosity or surface tension had changed during the coalescence experiments; no significant changes were observed.

Experimental Procedure

Bubble pairs of equal size were used in all coalescence experiments. To fix the bubble size, the distance between the electrode faces was set to twice the desired bubble diameter. Gap distances were determined to within 2% of the total gap width, as observed on the video monitor.

To generate electrolytic bubbles, a current of approximately 30 μA was applied for a few minutes to grow the bubbles until they came close to contacting each other. During this time, the potentiometer was adjusted to control the relative current to each electrode to ensure that the bubbles were of equal size. Growth continued for another few minutes at a current of approximately 3 μA until light from the fiber optic source no longer passed between the bubbles into the microscope. Since the shadows of the bubbles became visible on the face of the detector once they had grown into the laser light sheet, final positioning of the bubbles relative to the detector was confirmed by observing the image itself. Growth up to coalescence was accomplished by applying a trickle current of less than 1 μA for about 30 s. During this final growth period, no positioning adjustments were made and no contact was made with the optics table. Coalescence automatically triggered the detector circuitry.

For most of the experimental conditions used, two sets of data were collected: one at a low sampling rate to capture the long-time behavior and another at a sampling rate of 1×10^6 samples per second to capture the initial motion of the interface. Typically, data from 15 to 20 bubble pairs were collected at each sampling rate. After a given bubble pair coalesced, the electrolytic cell was moved vertically so that the subsequent coalescence event would be recorded by a different set of photodiode elements. By rastering the shadows of consecutive bubble pairs up and down the array in this way and averaging the results, smooth position vs. time curves were obtained.

The initial velocity of the saddle point and the period and damping rate of its oscillations were determined using curves like those in Figure 3. The oscillation period was read to the nearest 0.05 ms, corresponding to the nearest 3% for the largest bubbles examined in the experiments and 20% for the smallest. The damping rate was determined to the nearest 0.01 ms^{-1} for the largest bubbles and to the nearest 0.2 ms^{-1} for the smallest bubbles, corresponding to 2 and 8% precision, respectively. The initial velocity was measured to the nearest 0.25 m/s for all bubbles sizes, or to within 6 to 13% over the range of bubble sizes examined. Errors in the position and time measurement by the photodetector were negligible compared to the errors associated with reading the saddle-point curves. Small random variations in the saddle-point position stemming from the discrete binary output of the photodiode elements gave the curves a rough appearance.

Results

The motion of the lower saddle point of two coalescing 375-μm hydrogen bubbles in 1-M H_2SO_4 is shown in Figure 3, where the data are an average of the results for 40 different bubble pairs, 20 pairs sampled at a rate of 1×10^6 time steps per second for the first 60 μs and 20 pairs at a lower sampling rate of 9.1×10^4 steps per second. Zero time corresponds to the first time step during which motion was detected.

Once coalescence begins, the saddle point moves away from the line of centers of the two initial bubbles as the cusp of the resultant bubble opens. The surface energy decreases as the curvature and surface area of the cusp decrease and kinetic energy is imparted to the surrounding liquid. The data used to compute the initial velocity are shown in Figure 3b, which has an expanded time scale; the first eight data points were fit with a least-squares regression line to determine the slope, which in this case gives an initial velocity of 3.6 m/s. It is important to note that the rapid events as the hole first forms cannot be captured by this experiment, and the extrapolated initial radius of the hole is finite; the initial velocity recorded here is therefore the velocity reached after the ini-

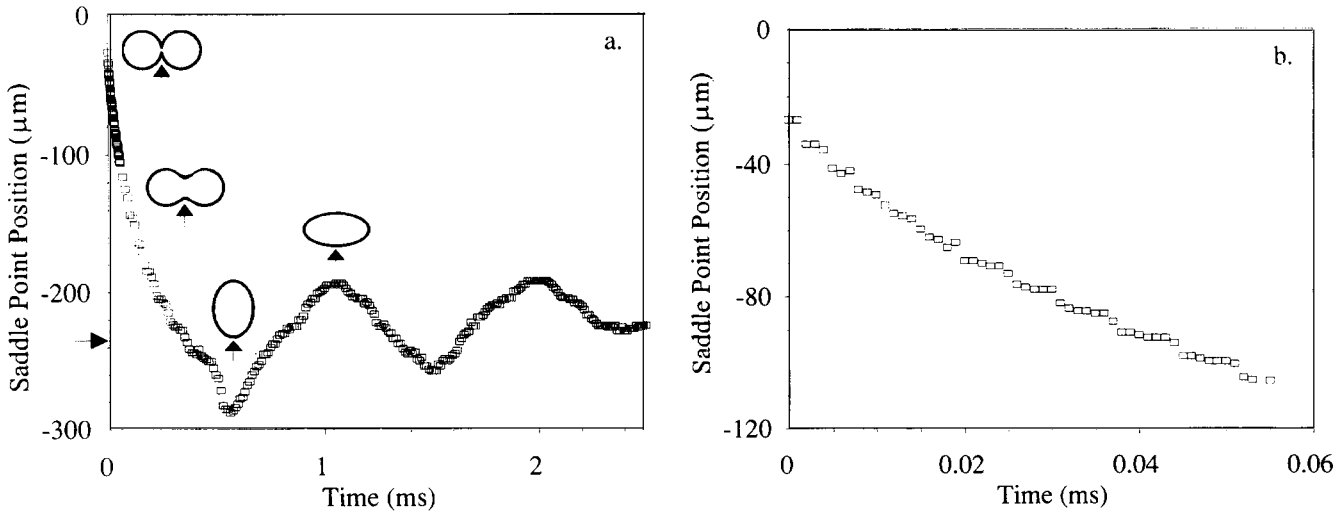

Figure 3. (a) Saddle point position as a function of time for 375-μm bubbles in 1-M H_2SO_4; (b) expanded scale for short times.

tial acceleration. The final bubble has a radius of 236 μm, indicated with an arrow on the position axis in Figure 3a. The interface oscillates about this equilibrium position as the bubble oscillates between prolate and oblate spheroidal shapes. The time between amplitude peaks in Figure 3a is 0.94 ms, while the damping rate (the time constant of the exponential decay of the amplitude) is 0.54 ms^{-1}.

Small-amplitude interfacial movements superimposed on the primary motion of the saddle point can be identified in Figure 3a. At about 0.40 ms, the saddle point appears to decelerate sharply, then to accelerate at about 0.45 ms. A qualitatively similar but smaller deceleration and acceleration occur at about 0.8 ms. These small amplitude movements are indications of surface waves.

The bubbles detach from the electrodes after coalescence begins, and the resultant bubble rises in the gravitational field, causing the net upward slope of the oscillations in Figure 3a. A comparison of the motions of the upper and lower saddle points of coalescing bubbles showed that buoyant motion occurred sufficiently slowly that it had no influence on the measured initial saddle-point velocity. The lower saddle point is used throughout this study.

Hydrogen bubble pairs with diameters of 50, 150, 375 and 600 μm were evolved in 1-M H_2SO_4. Saddle point data are shown in Figure 4, where it can be seen that the oscillation period increases and damping decreases with increasing bubble size. Large bubbles have higher initial saddle-point velocities than small bubbles, but the differences are small. The saddle-point displacements and initial velocities for the 375- and 600-μm bubbles are larger than those reported by Egan and Tobias (1994) for 500- and 625-μm bubbles, possibly because their origin for displacement was uncertain and their placement of the beam sheet was less precise.

The kinematic viscosity of 1-M H_2SO_4 electrolyte was raised to 3.0 and 5.0×10^{-2} cm^2/s by adding dextran [$(C_6H_{10}O_5)_x$, 40,000 molecular weight] to concentrations of 6 and 10 wt. %, respectively. The coalescence of 375-μm bubbles in high and low viscosity electrolyte is compared in Figure 5. Increasing the viscosity increases the damping rate with only a slight effect on the oscillation period and initial velocity, suggesting that damping is controlled by viscous resistance in the fluid surrounding the oscillating bubble.

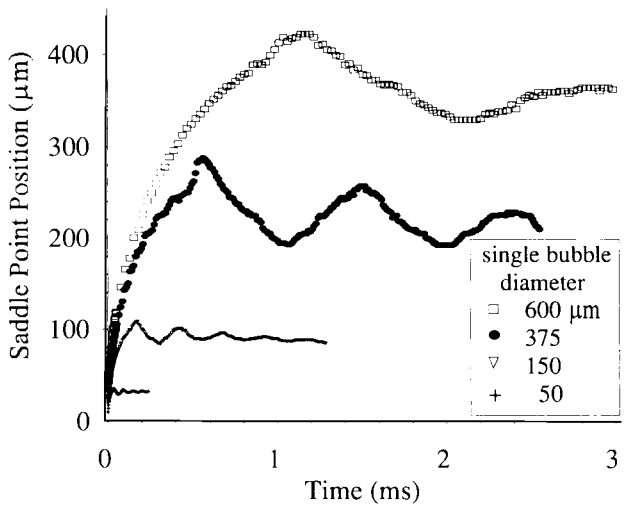

Figure 4. Saddle point position as a function of time for bubbles of different sizes.

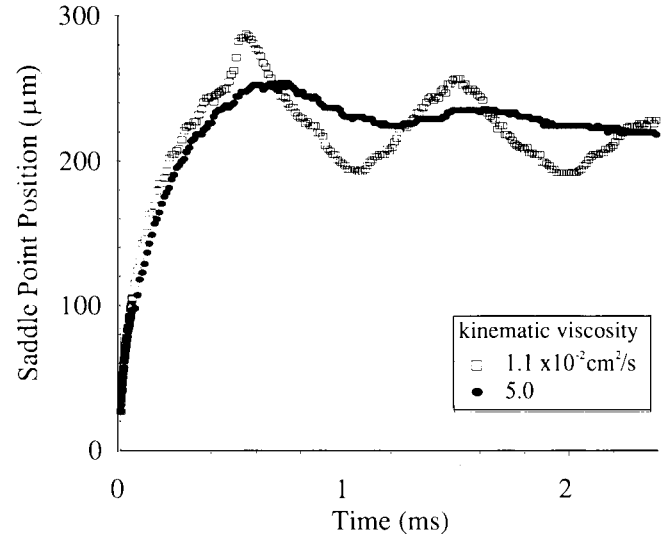

Figure 5. Saddle point position as a function of time for 375-μm bubbles in 1-M H_2SO_4 with added dextran to change the kinematic viscosity.

The surface tension of 1-M H_2SO_4 was reduced to 49 and 25 mN/m with the addition of 2-hexanol to concentrations of 0.001 and 0.07 M, respectively. The results in Figure 6 show that the oscillation period increases substantially with the lowering of surface tension, but there is no effect on damping and only a slight effect on the initial velocity.

Oxygen bubbles were generated by applying a positive current to one or both of the microelectrodes. The initial velocities, damping rates, and oscillation periods for different pairings of hydrogen and oxygen bubbles (H_2-H_2, H_2-O_2, or O_2-O_2) were the same within experimental uncertainty. Oxygen bubbles were generated in 1-M H_2SO_4 and 2-M KOH to examine the effects of electrolyte pH on bubble coalescence.

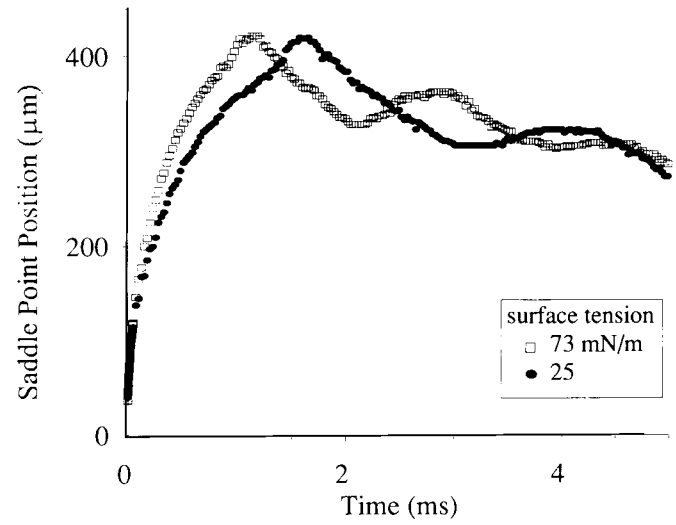

Figure 6. Saddle point position as a function of time for 375-μm bubbles in 1-M H_2SO_4 with added 2-hexanol to change the surface tension.

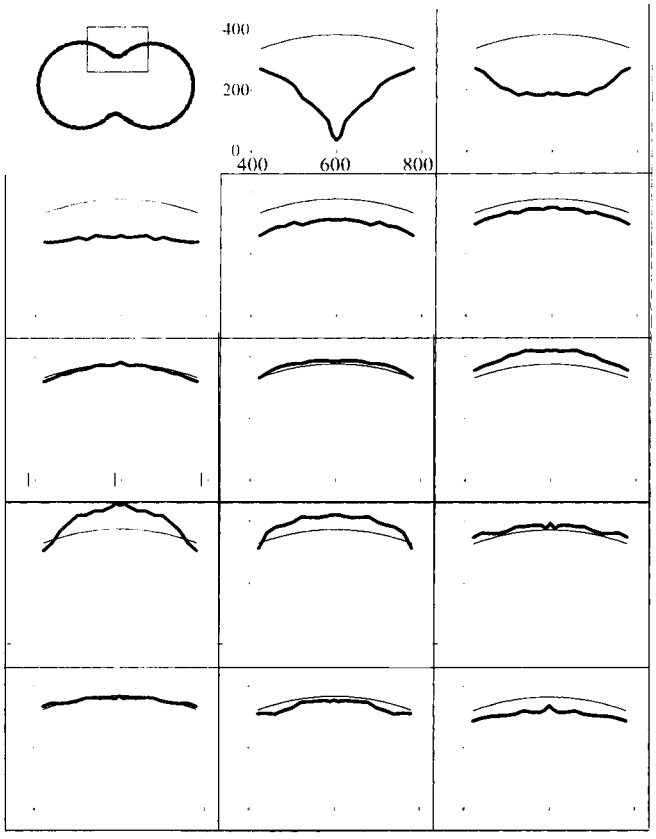

Figure 7. Interface motion near the saddle point of coalescing 600-μm bubbles.

The heavy line connects 20 points collected at approximately 0.063 ms/frame; the light line indicates the equilibrium position of the resultant bubble interface. Each frame represents 0.147 ms of elapsed time.

Despite the slightly higher surface tension and kinematic viscosity of 2-M KOH, the results demonstrated no measurable difference between coalescence events as a function of pH.

The two-dimensional representation of the saddle-point region of two coalescing 600-μm bubbles in Figure 7 was generated by recording interface motion as a function of time at eleven locations on one side of the saddle point and mirroring to provide symmetric images. Surface waves, especially visible in the second frame of the sequence, start as interfacial deformations near the saddle point at the onset of coalescence. Their impact on the motion of the saddle-point in Figure 3a was noted at 0.4 and 0.8 ms.

Scaling

If we assume that the initial velocity v_o of the saddle point is determined by an exchange between potential (surface) and kinetic energy and ignore viscous dissipation and curvature, it follows from dimensional analysis that

$$v_o = k(\sigma/\rho h)^{1/2} \tag{1}$$

where σ is the surface tension, ρ is the liquid density, h a length scale of the order of the liquid film between the bubbles just prior to coalescence, and k a constant. Culick (1960), generalizing a result of Dupré (1868) to include the inertia of the liquid of the film, calculated $k = \sqrt{2}$. This result is used in Egan and Tobias' (1994) modification of an analysis of Charles and Mason (1960) to obtain a differential equation for the evolution of the radius of the hole between the bubbles. The experimental values of v_o are of the order of meters per second (cf. Figure 3b), requiring initial film thicknesses of the order of tens of microns, which is clearly unrealistic, and the Egan and Tobias analysis does not agree well with the data; comparisons in Stover (1996) show that the experimental deceleration is much faster than predicted by the analysis.

It helps to think the oscillating bubble as a slightly deformed sphere, where surface tension acts as a restoring force, the surrounding fluid provides the mass, and viscosity damps the motion. The one-dimensional motion of the interface can then be modeled as a damped harmonic oscillator in which the mass is proportional to the bubble volume and the liquid density, the friction is proportional to the bubble cross-sectional area and the liquid viscosity, and the restoring force is proportional to the bubble-cross-sectional area, the curvature, and the surface tension. In the limit $\nu(\rho/R\sigma)^{1/2} \to 0$, where ν is the kinematic viscosity and R is the radius of the resultant bubble, the displacement of the oscillator has a period proportional to $(\rho R^3/\sigma)^{1/2}$ and an exponential damping factor proportional to ν/R^2. [The group $\nu(\rho/R\sigma)^{1/2}$ is known as the *Ohnesorge number*, *Oh*. The coalescence experiments were conducted over a range of *Oh* from 0.006 to 0.06.] The data in Figures 4 through 6 in general agree with this scaling: the oscillation period did not vary significantly despite a five-fold change in kinematic viscosity, smaller bubbles and higher viscosities resulted in faster damping, and lower surface tension and larger bubble size resulted in a longer period. A more detailed comparison is made subsequently.

Numerical Analysis

The dynamics of coalescence were simulated by solution of the transient Navier-Stokes equations for the liquid phase using FIDAP version 7.52, a general-purpose finite-element program supplied by Fluid Dynamics International. The program was run on a Hewlett Packard Model 715 workstation with an HP-UX version 9.03 operating system. Gravity was neglected and the domain was taken to be axisymmetric about the line of centers of the two original bubbles. The interfacial boundary conditions were tangential stress equal to zero and normal stress balanced by surface tension (the Young-Laplace equation). The initial shape for all simulations, approximated as an inverse ellipse with $m = 0.99$ (Hopper, 1984) to correspond to two bubbles with a small hole in the separating film, is shown in Figure 8; length was scaled in all cases by the final bubble radius ($2^{1/3}R$). The initial velocity was taken in all cases to be zero. A typical finite-element mesh is shown in Figure 9. Details of the simulation are in Stover (1996).

In the experiments, the bubbles were initially in contact with the electrode surfaces. Convergent simulations could, however, be obtained only when the bubbles were at least $0.26R$ from the solid boundary. Figure 10 shows a comparison of simulations for 600 μm-diameter bubbles initially placed $0.26R$ and $12.3R$ from the boundary, and it is clear

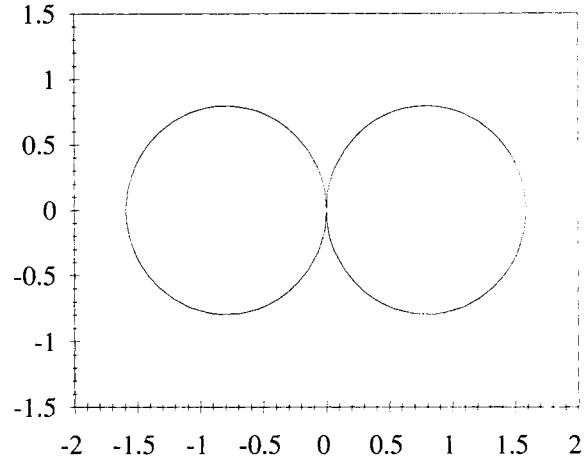

Figure 8. Initial condition for simulations; inverse ellipse with $m = 0.99$.

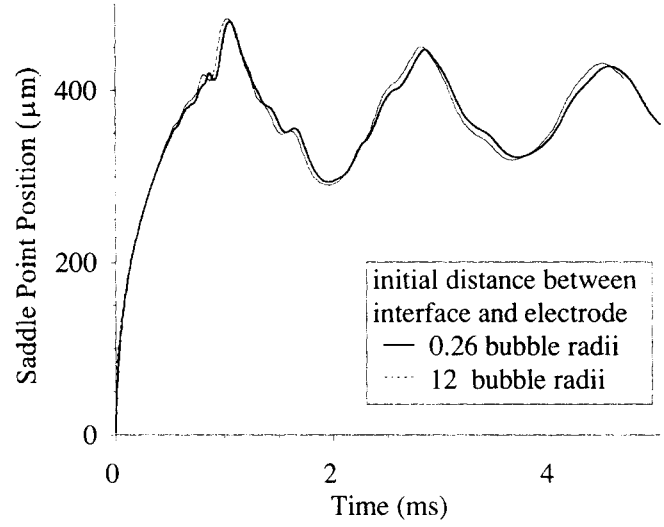

Figure 10. Effect of assumed location of electrode on simulation of 600-μm bubbles coalescing in 1.1×10^{-2} cm^2/s, 73 mN/m liquid (1-M H_2SO_4).

that the response is insensitive to the location of the wall in this range. The limiting behavior as the spacing goes to zero, however, is untested.

The simulated saddle-point-motion is compared to experimental data in Figure 11 for 375-μm bubbles coalescing in 1.1×10^{-2} cm^2/s, 73 mN/m electrolyte. The slope of the computed saddle-point motion in Figure 11a near time zero corresponds to a velocity of approximately 3.9 m/s, compared to the measured value of 3.6 m/s. (The slope precisely at time zero must be zero, since the initial velocity is set to zero in the simulation.) The period of 0.86 ms for the simulated oscillations is slightly less than the experimental value of 0.94 ms. The computed damping rate is 0.48 ms^{-1}, compared to the experimental value of 0.54 ms^{-1}. The simulation captures the shoulders (shown as small peaks) superposed on the primary peaks that indicate the movement of surface waves through the saddle point region. The small waves seen during the first 20 μs on the expanded scale in Figure 11b had the same appearance in simulations using higher mesh densities and smaller time steps. The experimental data begin at a position of 27 μm; the laser beam did not illuminate the saddle-point initially because the beam waist has a finite width and the cusp is extremely narrow.

Simulations were carried out for bubble sizes of 50, 150, 375 and 600 μm for the kinematic viscosities and surface tensions used in the experiments. Detailed results are in Stover (1996). The experimental and computed damping rates are shown in Figure 12 as a function of ν/R^2. The simulations follow the harmonic oscillator scaling quite well, whereas the data follow the scaling at small values of the ordinate. The computed and measured oscillation periods are shown in Figure 13, where it is seen that both experiments and simulations follow the oscillator scaling. The short-time velocity computed from the simulations, shown in Figure 14, is proportional to $(\sigma/\rho R)^{1/2}$, which is consistent with the fact that the simulation begins with a zero initial velocity and a small hole already in place with a diameter that scales with R; the experimental initial velocities show no trend with $(\sigma/\rho R)^{1/2}$.

The simulations provide two-dimensional images of the bubble interface. The series of frames in Figure 15 shows the evolution of the interface with time after two 600-μm bubbles have coalesced. The experimental data are in good agreement with the computed results for the interface near the coalescence plane. The large wave created by the initial motion of the cusp travels around the interface and eventually returns to the coalescence plane.

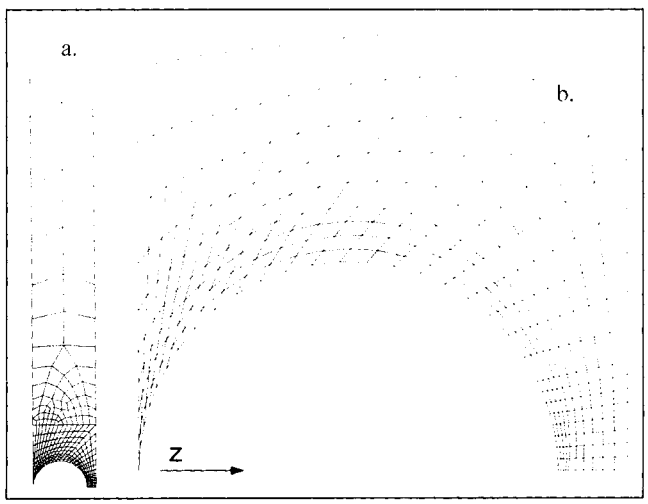

Figure 9. Finite-element mesh.

(a) Full domain (only one-fourth of the spatial domain is required because of symmetries); (b) magnified view near bubble.

Conclusions

The generally good agreement between the experiments and simulations supports the following scenario for electrolytic bubble coalescence: Following rupture of the film separating the bubbles, the surface energy decreases as the curvature and surface area of the resultant bubble decrease, and the kinetic energy is imparted to the surrounding liquid.

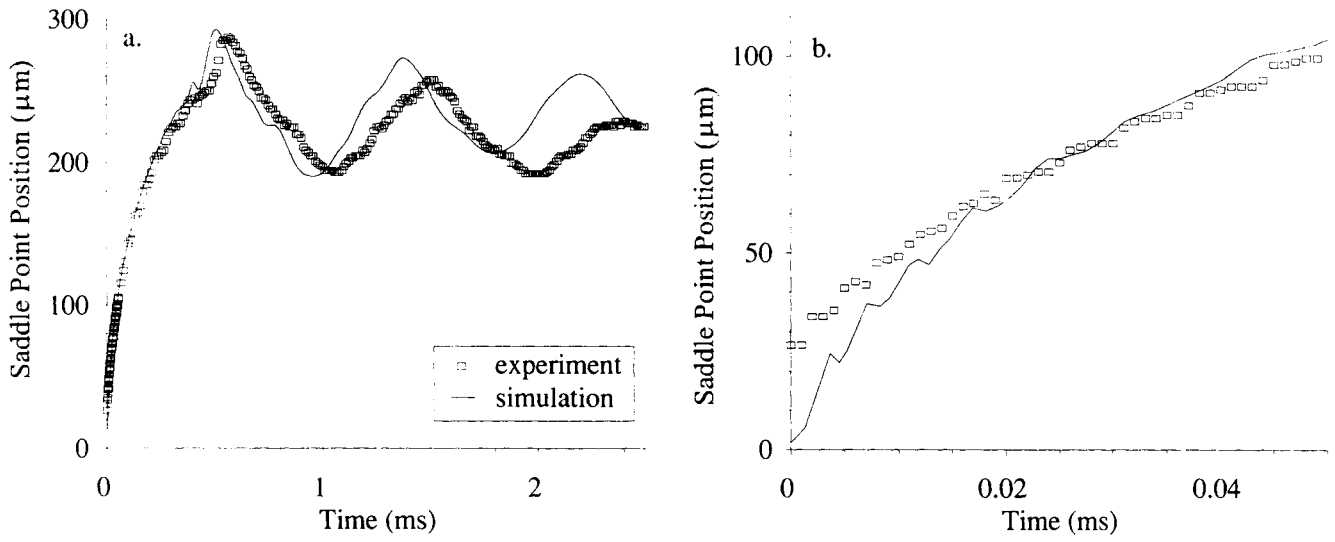

Figure 11. (a) Computed and experimental saddle point motion of 375-μm bubbles coalescing in 1.1×10^{-2} cm²/s, 73 mN/m liquid (1-M H_2SO_4); (b) expanded scale for short times.

The initial motion is driven by the surface tension and slowed by the inertia and viscosity of the surrounding fluid. Fluid inertia sustains the oblate/prolate oscillations of the resultant bubble and viscous resistance dampens the oscillations. Surface waves are superimposed on the motion of the bubbles, and while they are likely to enhance mass transfer they have little effect on the overall dynamics. Within the viscosity range studied, the period is insensitive to the viscosity and damping is insensitive to surface tension. Coalescence does not depend on gas type (electrode polarity) or electrolyte pH.

There are two major discrepancies between the simulations and the experiments. The failure of the simulations to reflect the initial motion as recorded by the laser system is a consequence of limitations of both the experiments and the simulations; the experiments cannot capture the initial events at rupture, while the simulations of necessity start after rupture and with an unrealistic initial condition on the velocity field. The poor agreement between experimental and calculated damping rates at the larger values of ν/R^2 is, however, a cause for concern. Good agreement between the simulations and experiments was obtained in the 1-M H_2SO_4 for 600-μm bubbles using the measured surface tension of 73 mN/m, but good agreement was obtained for the smaller bubbles only by reducing the surface tension in the simulations to 60 mN/m for 375-μm bubbles and to 49 mN/m for 150-μm bubbles (Stover, 1996). Since the electrolytic cell was open to the atmosphere, it is possible that the surface tension changed with time as surface-active species accumulated on the bubbles (Levich, 1962; Kelsall et al., 1996). Small bubbles would have been affected to a greater degree, because less surface-active material would be required to alter their sur-

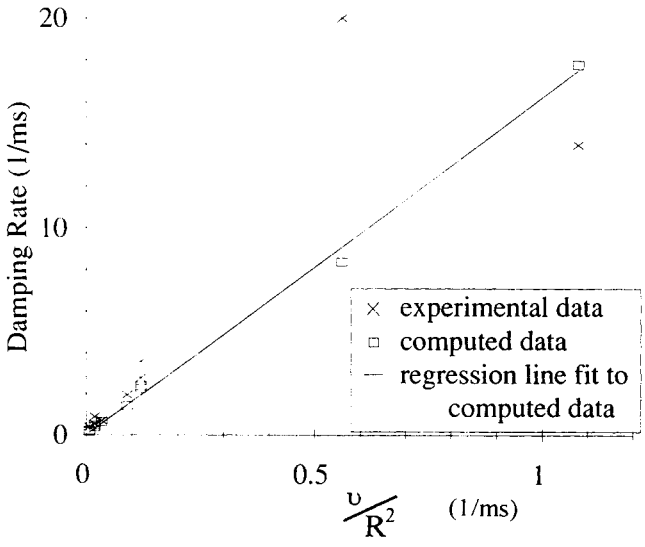

Figure 12. Damping rate as a function of ν/R^2.

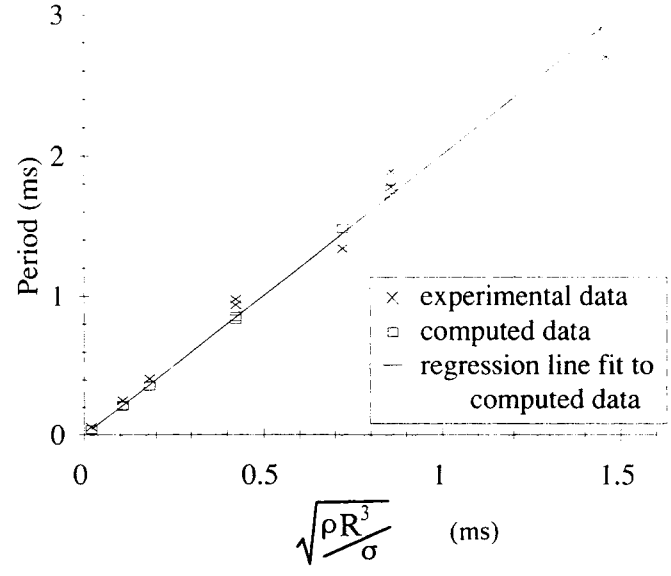

Figure 13. Period as a function of $(\rho R^3/\sigma)^{1/2}$.

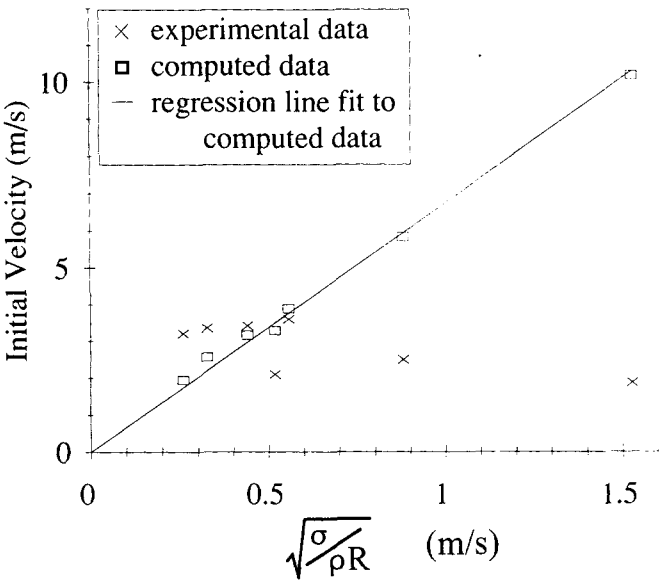

Figure 14. Initial velocity in 1.1×10^{-2} cm²/s liquid as a function of $(\sigma/\rho R)^{1/2}$.

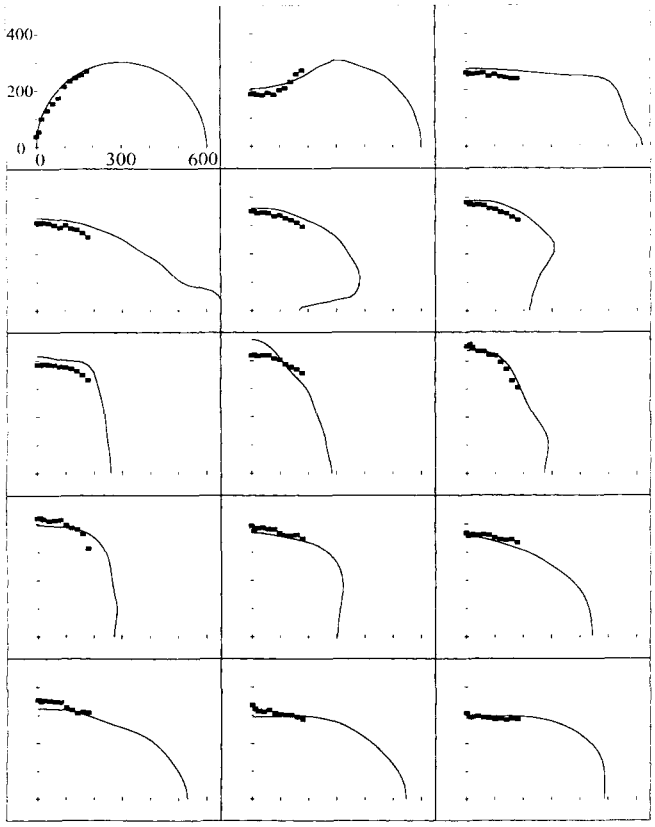

Figure 15. Two-dimensional representation of bubble interface.

Each frame shows one-quarter of the interface of two coalescing 600-μm bubbles in 1.1×10^{-2} cm²/s, 73 mN/m liquid (1-M H_2SO_4). The squares are experimental data, while the line is the simulation. Each frame represents 0.147 ms of elapsed time.

face concentrations, and because the experiments with small bubbles required several hours while the experiments with large bubbles were completed in less than one hour. This explanation is speculative, however.

Acknowledgment

This work was supported in part (RLS and CWT) by the Assistant Secretary for Energy Efficiency and Renewable Energy, Office of Transportation Technologies, Office of Advanced Automotive Technologies of the U.S. Department of Energy, and in part (MMD) by the Director, Office of Energy Research, Office of Basic Energy Sciences, Materials Science Division of the U.S. Department of Energy, under Contract No. DE-AC03-76SF00098.

Literature Cited

Basaran, O. A., "Nonlinear Oscillations of Viscous Liquid Drops," *J. Fluid Mech.*, **241**, 169 (1992).

Charles, G. E., and S. G. Mason, "The Coalescence of Liquid Drops with Flat Liquid/Liquid Interfaces," *J. Coll. Sci.*, **15**, 236 (1960).

Chi, B. K., and L. G. Leal, "A Theoretical Study of the Motion of a Viscous Drop toward a Fluid Interface at Low Reynolds Number," *J. Fluid Mech.*, **201**, 123 (1989).

Culick, F. E. C., "Comments on a Ruptured Soap Film," *J. Appl. Phys.*, **31**, 1128 (1960).

Dees, D., and C. W. Tobias, "Mass Transfer at Gas Evolving Surfaces," *J. Electrochem. Soc.*, **134**, 1702 (1987).

DeVries, A. J., "Foam Stability," *Recueil*, **77**, 383 (1958).

Dupré, A., *Theorie Mecanique de la Chaleur*, Gauthiers-Villars, Paris (1868).

Egan, E. W., and C. W. Tobias, "Measurement of Interfacial Reequilibration during Hydrogen Bubble Coalescence," *J. Electrochem. Soc.*, **141**, 1118 (1994).

Frankel, S., and K. J. Mysels, "The Bursting of Soap Films. II. Theoretical Considerations," *J. Phys. Chem.*, **73**, 3018 (1969).

Hopper, R. W., "Coalescence of Two Equal Cylinders: Exact Results for Creeping Viscous Plane Flow Driven by Capillarity," *Communications of the American Ceramic Society*, p. C-262 (Dec., 1984).

Janssen, L. J. J., and J. G. Hoogland, "The Effect of Electrolytically Evolved Gas Bubbles on the Thickness of the Diffusion Layer," *Electrochim. Acta*, **18**, 543 (1973).

Kelsall, G. H., S. Y. Tang, A. L. Smith, and S. Yurdakul, "Measurement of Rise and Electrophoretic Velocities of Gas Bubbles," *J. Chem. Soc., Faraday Trans.*, **92**, 3879 (1996).

Levich, V. G., *Physiochemical Hydrodynamics*, Prentice-Hall, Englewood Cliffs, NJ (1962).

Marrucci, G., "A Theory of Coalescence," *Chem. Eng. Sci.*, **24**, 975 (1969).

Oolman, T. O., and H. W. Blanch, "Bubble Coalescence in Stagnant Liquids," *Chem. Eng. Commun.*, **43**, 237 (1986).

Patzek, T. W., R. E. Brenner, Jr., O. A. Basaran, and L. E. Scriven, "Nonlinear Oscillations of Inviscid Free Drops," *J. Comp. Phys.*, **97**, 489 (1991).

Putt, R., "Studies of the Events Occurring at Gas-Evolving Electrodes," MS Thesis, Univ. of California, Berkeley (1975).

Sides, P., and C. W. Tobias, "A Close View of Gas Evolution from the Back Side of a Transparent Electrode," *J. Electrochem. Soc.*, **132**, 583 (1985).

Stover, R. L., "Bubble Coalescence Dynamics and Supersaturation in Electrolytic Gas Evolution," PhD Diss., Univ. of California, Berkeley (1996); E. O. Lawrence Berkeley National Laboratory Report LBNL-39258 (Aug., 1996).

Manuscript received Feb. 18, 1997, and revision received July 3, 1997.